Chromium-doped zinc gallate: Impact of Sn4+ co-doping on the persistent luminescence properties at the nanoscale applied to bio-imaging

Guanyu Cai, Johanne Seguin, Thomas Naillon, Corinne Chanéac, Yohann Corvis, Daniel Scherman, Nathalie Mignet, Bruno Viana, Cyrille Richard

Chromium-doped zinc gallate: impact of Sn^{4+} co-doping on the persistent luminescence properties at the nanoscale applied to bio-imaging

Authors

Guanyu Cai [1,2], Johanne Seguin [2], Thomas Naillon [1,3], Corinne Chanéac [3], Yohann Corvis [2], Daniel Scherman,[2] Nathalie Mignet [2], Bruno Viana [1,*] and Cyrille Richard [2,*]

Addresses

1. PSL University, CNRS, IRCP, Institut de Recherche de Chimie Paris, Chimie ParisTech, 75005 Paris, France
2. Université Paris Cité, CNRS, INSERM, UTCBS, Unité de Technologies Chimiques et Biologiques pour la Santé, Faculté de Pharmacie, 75006 Paris, France
3. Laboratoire de Chimie de la Matière Condensée de Paris (LCMCP), Sorbonne Université, CNRS, 75005 Paris, France

Corresponding author Email :

cyrille.richard@u-paris.fr (C.R.); bruno.viana@chimieparistech.psl.eu (B.V.)

Abstract

Persistent luminescence (PersL) nanoparticles emit a signal that lasts long after the excitation has ended, enabling highly sensitive bioimaging without background noise. When using UV light as excitation source before the injection, a strong PersL signal can be detected *in vivo* before disappearing within a few hours. For long-term imaging, we have shown in the past that visible LED can be used to re-excite $ZnGa_{1.995}Cr_{0.005}O_4$ ($ZGO:Cr^{3+}$) nanoparticles *in vivo*, producing a signal intensity that is, however, much lower compared to the signal obtained after the UV pre-excitation method. This lower signal intensity of the nanoprobe when using visible LED may prevent its detection in some cases. Herein, we report an improvement in the excitation efficiency of visible LED using $Zn_{1.33}Ga_{1.335}Cr_{0.005}Sn_{0.33}O_4$ ($ZGSO:Cr^{3+}$) PersL nanoparticles. We fully compared $ZGSO:Cr^{3+}$ and original ZGO:Cr in term of structure, optical properties and bio-imaging potential. The co-doping with tin strongly enhances the persistent luminescence, even at the nanoscale. *In vivo* imaging results showed that $ZGSO:Cr^{3+}$ exhibits an approximately 3-fold signal enhancement compared to $ZGO:Cr^{3+}$ using UV pre-excitation. Even more interestingly, when using LED excitation, the signal intensity of ZGSO: Cr^{3+} is more than 10-fold higher than the one of $ZGO:Cr^{3+}$, making ZGSO nanoparticles much easier to detect. ZGSO:Cr nanoparticles can be surface-modified with PEG to get nanoprobes with a much longer residence time in blood. This unique comparison between both compositions makes $ZGSO:Cr^{3+}$ a more effective imaging diagnostic probe than the original $ZGO:Cr^{3+}$ nanoparticles, opening up new applications for *in vivo* diagnostics.

Highlights:

- ZGSO:Cr^{3+} NPs emit 10-fold enhanced PersL compared to original ZGO:Cr^{3+}
- Improvement of PersL imaging *in vivo*;
- High efficacy of *in situ* excitation using visible light (LED).

Graphical Abstract

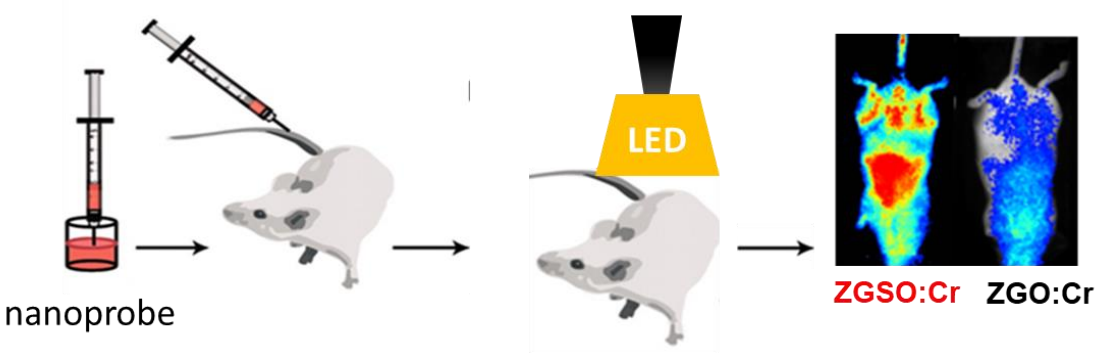

1. Introduction

Persistent luminescence (PersL) materials can absorb and store the photoexcitation energy into traps, before slowly releasing it in the form of a PersL signal that lasts for a relatively long duration (minutes to hours) after the excitation has been stopped [1-6]. This intriguing optical feature has attracted extensive attention in various fields such as imaging [7] and lighting [8-10]. Recently, near-infrared (NIR) PersL nanoparticles (NPs), as a new type of luminescent probes, have been widely applied in biology when prepared at the nanoscale for imaging [7, 11-16] diagnosis [17-20] and therapies [21-28], and even in other broader fields [29-32]. Compared to traditional fluorescence imaging, bioimaging using NIR PersL NPs exhibits a higher signal-to-noise ratio (SNR) due to less background noise [33]. For such application, the PersL nanoprobes can be pre-excited before their injection with ultraviolet (UV) light, for example when using silicate NPs doped with Eu, Dy, Mn [12], phosphate NPs doped with Eu, Dy, Mn or nitridosilicate NPs doped with Eu, and Tm [34]. Although various PersL NPs compositions and other excitation sources varying from X-rays to visible light [35-40] have been widely used, the re-excitation efficiency *in vivo* is still an issue due to the limited tissue penetration of the excitation light, particularly when using UV or visible light sources [41].

In the past, we have shown that $ZnGa_{1.995}Cr_{0.005}O_4$ (ZGO:Cr) is a safe and very effective nanoprobe for bioimaging [41-43]. However, a limit of this probe is the limited efficiency of the *in vivo* LED excitation [41], meaning that the signal obtained after LED excitation, either to (i) photostimulate and release already filled deep traps [44] or (ii) favor the creation of traps, is much lower than after UV pre-excitation, differing by about one log in intensity [41, 43]. This may prevent the detection of the nanoprobe, especially if present in small amount [43]. It has been demonstrated that enhancement of the LED excitation of ZGO:Cr^{3+} can be obtained by co-doping the zinc-gallate host with various tetravalent cations such as Ge^{4+} [45] or Sn^{4+} [46, 47] increasing defect formation. Pan *et al* [46] for instance reported an enhancement in the first minutes of the persistent decay. However, such observation was reported at the bulk scale with materials prepared using a solid state method, preventing their administration as a suspension *in vivo*.

In the present study, we report the synthesis of $Zn_{1.33}Ga_{1.335}Cr_{0.005}Sn_{0.33}O_4$ (ZGSO:Cr) at the nanoscale, using a hydrothermal method followed by an annealing at 750°C and a ball milling process. After the extraction of 90-nm size nanoparticles, the signal intensity of

ZGSO after UV or visible LED light excitation was compared to the original ZGO:Cr NPs, strictly prepared under the same conditions. Thus, it has been proved that a better efficiency is always obtained for ZGSO:Cr NPs, both in dry form and in suspension, underling the environmental impact on luminescence efficiency. More importantly, it was possible to get a 10-fold signal intensity improvement with ZGSO vs ZGO using LED as the excitation source. To evaluate the efficiency of ZGSO:Cr NPs in regards to ZGO:Cr NPs, signals emitted by both NPs through different layers of tissues, as well as *in vivo* using mice were performed. Compared to what was observed in the bulk [46], our results demonstrate that even at the nanoscale, visible LED can efficiently excite ZGSO:Cr NPs to produce a NIR PersL signal, up to 10-fold higher, offering an alternative of interest to ZGO:Cr NPs. These point by point comparison between ZGSO and ZGO, such as structure, optical properties, as well as the evaluation of the effect on bio-imaging in deep tissue and in vivo, makes $Zn_{1.33}Ga_{1.335}Cr_{0.005}Sn_{0.33}O_4$ (ZGSO:Cr) a superior nanoprobe to visible LED light excitation, highly promising for further *in vivo* imaging, after an appropriate surface functionalization.

2. Materials and methods

Chemicals

3-Aminopropyl-triethoxysilane (APTES) was obtained from Sigma-Aldrich. Zinc nitrate hexahydrate (>99%) was purchased from Fluka. Tin chloride (>99.9%), gallium oxide (99.999%), chromium (III) nitrate nonahydrate (99.99%), and dimethylformamide (>99.9%) were purchased from Alfa Aesar. Alpha-methoxy-omega-N-hydroxysuccinimide poly(ethylene glycol) PEG MW 5000 Dalton was bought from Iris Biotech GmbH.

2.1 Preparation of $ZGO:Cr^{3+}$ and $ZGSO:Cr^{3+}$ NPs

ZGO:Cr NPs were synthesized by the hydrothermal method as already published by our laboratory. First, gallium nitrate was formed by reacting 8.94 mmol of gallium oxide with 20 mL of nitric acid (35 wt.%) under hydrothermal conditions at 150 °C for 24 hours. Then, a mixture containing 0.045 mmol of chromium nitrate and 8.97 mmol of zinc nitrate in 10 mL of water was added to the previous solution of gallium nitrate under vigorous stirring. The resulting solution was adjusted to pH 7.5 with an ammonia solution (30 wt.%), stirred

for 3 hours at room temperature, and transferred into a 45 mL Teflon-lined stainless-steel autoclave for 24 h at 120 °C. The resulting solid was washed several times with water and ethanol before being dried at 60 °C for 2 hours. The dry white powder was finally sintered in air at 750 °C for 5 hours. Hydroxylation was performed by acid wet grinding of the powder (500 mg) for 15 minutes, with a mortar and pestle in 2 mL of 5 mM HCl solution, and vigorously stirred overnight at room temperature at 10 $mg.mL^{-1}$ in 5 mM HCl. The hydroxylated ZGO (ZGO-OH) NPs with a diameter ~ 90 nm were selected from the whole polydisperse colloidal suspension by centrifugation on a SANYO MSE Mistral 1000 at 4500 rpm for 10 minutes. ZGO NPs present in the supernatant were gathered and concentrated.

The synthesis of $Zn_{1.33}Ga_{1.335}Cr_{0.005}Sn_{0.33}O_4$ (ZGSO:Cr) was adapted from the synthesis of ZGO:Cr nanoparticles by a hydrothermal method with a subsequent calcination process [44]. In this method, 8.94 mmol of gallium oxide were dissolved in 10 mL of nitric acid (35 wt%) under hydrothermal conditions for 48 h at 150 °C. Then 10 mL of an aqueous solution containing 17.82 mmol of zinc nitrate hexahydrate, 4.42 mmol tin (IV) chloride pentahydrate, and 0.07 mmol chromium (III) nitrate nonahydrate were added to the vessel under vigorous stirring. The pH of the solution was adjusted to 7.5 using ammonia solution (30 wt%). The mixture was stirred for 3 h at room temperature, and then transferred into a stainless-steel autoclave before heated at 120 °C for 24 h in an oven. The resulting solid was washed several times with water and ethanol, dried at 60 °C for 2 h, and then sintered in air at 750 °C for 5 h. The obtained white powder was then ground in hydrochloric acid (5 $mmol.L^{-1}$), stirred overnight in HCl 5 mM, and centrifuged at 4500 rpm for 10 min, selecting the supernatant that had an average size of ~ 90 nm, following the same method as for ZGO:Cr NPs.

2.2 Functionalization of ZGO:Cr^{3+} and ZGSO:Cr^{3+} NPs

The surface of ZGO:Cr^{3+} NP and ZGSO:Cr^{3+} NPs was functionalized using the same method and parameters, using a slightly modified protocol we previously reported [41]. Following is an example using the ZGSO NPs. Briefly, ZGSO-NH_2 nanoparticles were prepared by adding 20 µL of 3-aminopropyl-triethoxysilane (APTES) to a suspension of 5 mg ZGSO-OH in 2 mL DMF. The reaction mixture was sonicated for the first 2 minutes

using a Branson Ultrasonic Cleaner 1210 and kept under vigorous stirring for 5 hours at room temperature. Then, the nanoparticles were washed from the unreacted APTES by three centrifugation and redispersion steps in DMF. ZGSO-PEG nanoparticles were prepared by reacting 10 µmol of MeO-PEG_{5kDa}-NHS (50 mg) with 5 mg of ZGSO-NH_2 nanoparticles in 2 mL DMF. To ensure a maximum PEG density, this functionalization step was achieved overnight, under vigorous stirring at 90°C.

2.3 Characterizations

2.3.1. X-ray Diffraction (XRD)

X-ray diffraction (XRD) patterns were obtained with an X-ray diffractometer (XPert PRO, Malvern Panalytical Ltd.,) equipped with a Ge111 single-crystal monochromator and by selecting the Kα1 radiation wavelength of the Cu X-ray tube (0.15405 nm). The two materials showed crystalline phases with cubic spinel structures.

2.3.2. Dynamic Light Scattering (DLS)

The hydrodynamic diameter of ZGO and ZGSO NPs was characterized by dynamic light scattering (DLS) performed with a Zetasizer Nano ZS (Malvern Instruments, Southborough, MA, USA) equipped with a 632.8 nm helium–neon laser and 5 mW power, with a detection angle of 173° (non-invasive backscattering). Zeta potentials were characterized using the same equipment and measurements were done in NaCl 20 mM.

2.3.3. Optical Spectroscopy

Absorption measurements of the dry ZGO:Cr and ZGSO:Cr NPs were carried out in a UV/Vis/NIR spectrophotometer (Varian Cary 6000i, Agilent). The resolution was 0.1 nm for the Cr bands. Visible and deep-red (or NIR-I) photoluminescence (PL) measurements of dry ZGO:Cr and ZGSO:Cr NPs were performed using an ICCD camera (Roper Pixis 100, Teledyne Princeton Instruments) cooled at −65 °C and coupled to a monochromator, with 300 grooves per mm and centered at 500 nm.

2.3.4. Persistent Luminescence and Thermoluminescence

The dry ZGO:Cr and ZGSO:Cr powder samples were thermally detrapped before each experiment by increasing the temperature up to 90 °C and then kept in the dark. Thermoluminescence (TL) measurements were performed using a closed-cycle Heflow cryostat (Sumitomo Cryogenics HC-4E) attached to a temperature controller (Lakeshore 340). The samples were firstly excited with a 365 nm lamp for 5 min at 10 K, and after excitation removal, the TL curves were recorded at a 10 K/min incline while heating up to 470 K. The signal was recorded using an ICCD camera (Roper Pixis 100, Teledyne Princeton Instruments) coupled to a visible monochromator (Acton Spectra Pro, Princeton Instruments), at 300 grooves per mm, centered at 500 nm. Typically, a measurement time of 1 hour was needed for the temperature-dependent luminescence intensity shown in this work.

2.3.5 Transmission electron microscopy (TEM) and Thermogravimetric analysis (TGA)

Transmission electron microscopy (TEM) images were obtained using a TecnaiSpiritG2 microscope operating at 120 kV. 5 µL of each suspension at 1 mg/mL) have been dropped for 1 min and the grids have been wiped. TGA was performed by using a TGA/DSC 1 from Mettler-Toledo (Greifensee, Switzerland) sensitive to 1 µg and calibrated beforehand with internal standard weights. Dry samples of approximately 2 mg were analyzed in alumina pans with a central hole of 1 mm diameter. The experiments were performed at a heating rate of 5 K min^{-1}, under a dry air flow of 70 mL min^{-1}.

2.4 Deep tissue imaging

Two different procedures have been used: 1) pre-excitation and 2) *in situ* activation method. For the first procedure (Fig 4a and 5a), UV excited NPs (suspension at 2 mg/mL) were covered by 1-3 pieces of tissue (pork pieces with thickness ~ 2 mm / piece) and transferred into an Optima camera (Biospace Lab) for a PersL signal detection for 5 minutes. For the *in situ* excitation procedure (Fig 4c and 5c), PersL NPs covered by tissues (1-3 pieces were used) are excited using visible LED source (Philips Lumiled 70W 5700 lm equipped with 515 nm cut-off filter) for a 2 minutes charging time. Then, the Optima camera (Biospace Lab) camera is used for 5 min PersL signal acquisition.

2.5 In vivo imaging

Balb/cJRj female mice, eight weeks of age (18 ~ 22 g), were purchased from Janvier labs. *In vivo* experiments were approved by French National Ethics Reflection Committee on Animal Experimentation (Comité national de réflexion éthique sur l'expérimentation animale, CNREEA). UV pre-excited NPs were injected in retroorbital way by using insulin syringes (0.2 mL volume containing 10 mg/mL NP suspension in 5% glucose solution). At different time points after injection (~1 h, ~4 h), mice were irradiated for 2 min with visible LED light and then imaged for 5 min with the Optima camera (Biospace Lab). 4 hours after injection, animals were anesthetized with gaseous isoflurane and sacrificed by cervical dislocation. Liver, spleen, lungs, heart and kidneys were collected and placed on a black plate and irradiated with LED. Persistent luminescence decay curves were obtained with an Optima camera (Biospace Lab, France). The LED emission is covering the range from 515 to 700 nm, centered at ~600 nm, as shown in Fig. S2.

3. Results and discussion

3.1 Microscopic morphology of ZGO:Cr and ZGSO:Cr NPs

Transmission electron microscopy (TEM) was used to determine the morphology and microstructure of pristine ZGO:Cr NPs (Fig. 1a) and ZGSO:Cr NPs (Fig. 1b) and coated NPs (Fig 7g-h). These images show that particle sizes of both PersL NPs are similar, around 20 nm. Note that the interplanar spacing of the ZGSO:Cr [d (111) = 0.457 nm] (Fig. 1 c) is larger than for ZGO:Cr [d (111) = 0.444 nm] (Fig. 1 d), as Sn atoms, with larger radius than Ga atoms, may strongly enlarge neighboring atoms or ions, resulting in an increase interplanar spacing [46]. Indeed this leads to an expansion of the crystal lattice. The regular shape observed is due to a slow growth of nanocrystals in the hydrothermal reaction, and a high crystallinity of the compounds, as observed in the electron diffraction (ED) results of the single crystals (Fig. 1 e – f).

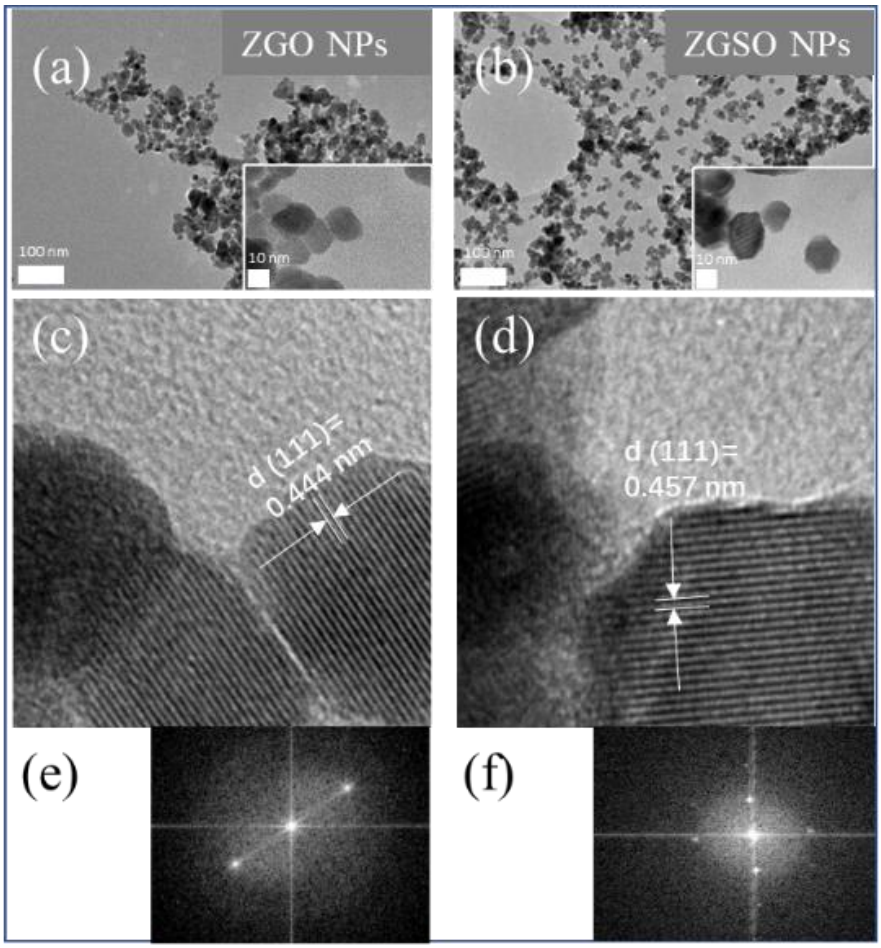

Fig. 1. TEM images of (a) ZGO:Cr^{3+} NPs and (b) ZGSO:Cr^{3+} NPs with size diameter ~ 20 nm; (c, d) lattice fringes of ZGO:Cr^{3+} NPs and ZGSO:Cr^{3+} NPs under the HRTEM; (e, f) the electron diffraction of ZGO:Cr^{3+} NPs and ZGSO:Cr^{3+} NPs. All illustrations are partial enlargement of the TEM images.

3.2 Physical properties of pristine NPs

The PL Excitation spectra of the ZGO:Cr^{3+} and ZGSO:Cr^{3+} spinel NPs are shown in Fig. 2 a. They show two broad excitation bands centered at ~ 550 nm and ~ 420 nm for the ZGO:Cr^{3+} and at ~ 580 nm and ~ 440 nm for the ZGSO:Cr^{3+}, which originate from the well-known $^4A_2(4F)\rightarrow{}^4T_2(4F)$ and $^4A_2(4F)\rightarrow{}^4T_1(4F)$ Cr^{3+} absorption transitions. The observed shoulders at ~ 300 nm are due to the $^4A_2(4F)\rightarrow{}^4T_1(4P)$ spin-allowed absorption band of Cr^{3+}, partially overlapping the band gap edge of the ZGO and ZGSO matrices [46, 48, 49]. Bandgap absorption edge originates from the O^{2-}-Ga^{3+} charge-transfer transition [46, 48]. Compared to ZGO:Cr^{3+}, the three mentioned absorption peaks are localized at longer

wavelengths in the ZGSO:Cr^{3+}, due to a decrease of the crystal field strength induced by tin insertion in the matrix. This will be favorable in the case of ZGSO:Cr^{3+} to longer wavelengths UV excitation but also to an orange excitation (coming from LED in the present work) as seen in the following part of the paper (Fig. 3a, c). With the presence of Sn^{4+} in the material, band gap absorption edge is red-shifted towards longer wavelengths.

The evolution of the PersL properties is presented in Fig. 2 b). Compared to ZGO:Cr^{3+}, ZGSO:Cr^{3+} presents a PersL spectrum with a red shifted emission (from 695 nm to 705 nm) and a broadening of the peak. The shifted emission towards the near infrared range is due to the Crystal Field variation to lower value. The broadening of the peak (FWHM is increasing from ~ 44 nm (ZGO:Cr emission) to ~ 61 nm (ZGSO:Cr emission)) is related to the enhanced contribution for the highest wavelengths of the Cr^{3+} $^4T_2 \rightarrow {}^4A_2$ transition, as the Sn^{4+}content increases. In addition, low temperature PL spectra (shown in Fig. S1 b) are well structured and composed of several sharp lines including R2 and N2 lines characteristic of chromium on the gallium octahedral site as reported in the literature [44, 48, 50]. When Sn^{4+} substitutes Ga^{3+}, several modifications of the PL spectra are observed. At first, Cr^{3+} emission lines strongly broaden with Sn^{4+} doping. This can be explained by the increased of the Cr^{3+} nearest-neighbors disorder as the Sn^{4+}content increases [46]. In parallel, a large contribution appears in the NIR range between 700 nm and 900 nm. The broadening of the emission band toward longer wavelengths attributed to the $^4T_2 \rightarrow {}^4A_2$ (Cr^{3+}) emission [51], is well supported by low temperature spectra (seen in Fig. S1 b). Furthermore, we noticed that N2 line is enhanced in ZGSO:Cr^{3+} as a consequence of Sn^{4+} doping in regard to the ZGO spinel matrix. Notice that the enhancement of the N2/R1 ratio is favorable to the PersL properties [44]. In addition, when the dry NPs are dispersed into water, the emission and excitation wavelength do not vary (as shown in Fig S1 a).

The optical properties of the NPs are dependent on their crystalline structure. XRD patterns of ZGO:Cr^{3+} and ZGSO:Cr^{3+} presented in Fig. 2 c) measured after calcination, before ball milling, suggest that both synthesized PersL NPs have a normal spinel structure, corresponding to the standard pattern of $ZnGa_2O_4$ (PDF No. 01-086-0413). Nevertheless, the diffraction peaks of ZGSO slightly shift to a lower angle for the $Zn_{1.33}Ga_{1.335}Cr_{0.005}Sn_{0.33}O_4$ NPs becoming closer to the diffraction peaks of Zn_2SnO_4 (PDF No. 01-073-1725), indicating that the unit cell parameters are intermediate to those of

$ZnGa_2O_4$ and Zn_2SnO_4 spinel materials. This corroborates the good tin insertion into the spinel host.

The difference of the optical properties between ZGO:Cr^{3+} and ZGSO:Cr^{3+} can explain the different thermoluminescence (TL) glow curves shapes as well. From the TL curves in Fig. 2 d, we observe for the TL peak responsible to the PersL (closer to room temperature) a less structured shape, coming with a decrease in temperature peak (T*m*) of the ZGSO:Cr^{3+}, compared to the ZGO:Cr^{3+} with a broadening of the glow curve due to the disorder since Sn^{4+} substitutes Ga^{3+} in ZGSO:Cr^{3+} nanocrystals. The shift in T*m* value from about 300 K to 260 K is in agreement with the smaller band gap of the ZGSO:Cr^{3+} as already reported in the bulk system [46]. This is also in agreement with the red shift of the absorption wavelength in the UV range [46, 48]. This can be related to the increasing number of Zn_{Ga}' defects. Namely additional defects such as Sn_{Ga}° appear. These defects can act as hole traps and electron traps respectively. In that case, an enhancement of PersL is expected due to the increased total traps capacity. This is indeed seen in Fig. 2 d (from the background level and the intensity axis scales). The total charging capability of the ZGSO:Cr^{3+} materials have been enhanced, as compared to the ZGO:Cr^{3+}. Trap depths can be calculated, using the following expression reported long time ago by Urbach and still widely used for the persistent phosphor [52-54]:

$$E_T = \frac{Tm}{500} \qquad \text{formula (1)}$$

The shift in T*m* values (Fig. 2d) from about 300 K to 260 K is in agreement with the smaller band gap energy for ZGSO:Cr in regards to ZGO:Cr. With formula (1), trap depth value is decreasing from 0.6 eV to 0.52 eV.

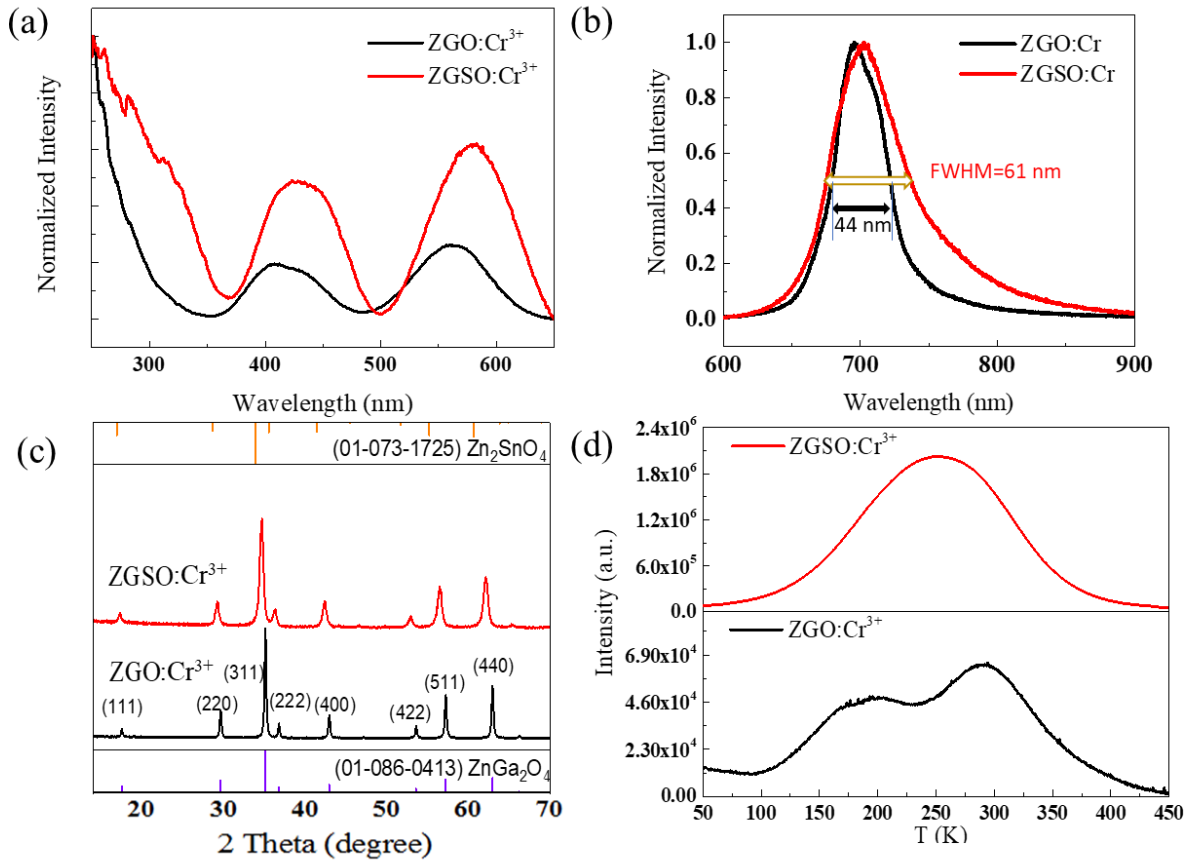

Fig. 2. (a) PL excitation spectra and (b) PersL spectra of ZGSO:Cr^{3+} NPs and ZGO:Cr^{3+} NPs. (c) X-ray diffraction pattern of ZGSO:Cr^{3+} (red curve) and ZGO:Cr^{3+} (black curve) and the two standard JCPDS cards of $ZnGa_2O_4$ and Zn_2SnO_4 materials. (d) Thermoluminescence (TL) glow curves of ZGSO:Cr^{3+} NPs (red curve) and ZGO:Cr^{3+} NPs (black curve). Notice the strong variation in the intensity scales.

3.3 Persistent luminescence properties of pristine NPs

To compare the PersL properties of ZGO:Cr NPs and ZGSO:Cr NPs, the first 5 min of PersL signal of both samples was collected as seen in Fig. 3, by monitoring Cr^{3+} emission at ~700 nm ($^2E \rightarrow {}^4A_2$ emission) after 2 min of photo excitation and waiting one minute before recording the PersL for each sample. When comparing the PersL after UV excitation of the two samples in dry NPs form in Fig. 3 a, the initial PersL signals in the same experimental conditions are about 1.4×10^5 counts for ZGSO:Cr NPs and about 4×10^4 counts for ZGO:Cr NPs. ZGSO:Cr NPs show ~ 3 times stronger NIR PersL signal. This result is

well supported by the TL results presented in the previous figure. As there are much more traps and released charges in ZGSO:Cr NPs, this causes stronger PersL, compared to ZGO:Cr NPs [46].

Not only UV but also visible orange LED light can be used as an excitation source for both dry NPs and dispersed NPs into water, both are presented in Fig. 2 and Fig. S1 a as well as in Fig. S2 for the PersL spectra. Orange LED source provides a broad emission peak centered at ~600 nm, as proposed in the illustration of Fig. S2 suggesting a better excitation of ZGSO sample due to its red shift of the $^4A_2(4F) \rightarrow {}^4T_2(4F)$ excitation band. This highlights the importance of matching excitation wavelengths with material properties especially using the low energy excitation towards localized antisite traps. Indeed, we can find that the initial PersL signals are ~ 5×10^3 counts for ZGO:Cr NPs and ~ 6×10^4 counts for ZGSO:Cr NPs in Fig. 3 b within the same experimental conditions. Thus, using visible LED excitation source, there is a ~ 12 times stronger PersL signal emitted by ZGSO:Cr NPs compared to ZGO:Cr NPs.

To further investigate the effect of solvent on the NIR PersL, the PersL signals of ZGSO:Cr^{3+} NPs and ZGO:Cr^{3+} NPs in water were collected at a concentration of 2 mg/mL. Interestingly, when dispersed into suspension, the presence of water leads to a significant decrease in PersL signal intensity for both ZGO and ZGSO under UV excitation due to water's strong UV absorption [55]. This underlines the environmental impact on luminescence efficiency. Fig. 3 c shows the NIR PersL (at ~ 700 nm) signal of both suspensions with respect to the decay time after irradiation/charging with UV light. Anyway, the larger amount of traps suggest about a 2-times stronger PersL signal emitted by ZGSO:Cr suspension compared to ZGO:Cr one.

Unlike UV, LED excitation in the orange/red range shows improved efficiency in water suspension, thanks to lower absorption by water[55]. This suggests visible LED excitation as a more effective approach for PersL applications in aqueous environments. With orange LED light excitation, much stronger NIR PersL can be detected during the first 5 min, which is a ~ 10 times stronger (around 5×10^4 counts) for the ZGSO:Cr suspension. These results suggest that the ZGSO:Cr NPs exhibit better PersL performance in suspension, which is particularly interesting for further *in vivo* imaging experiments that will use visible/orange LED light excitation.

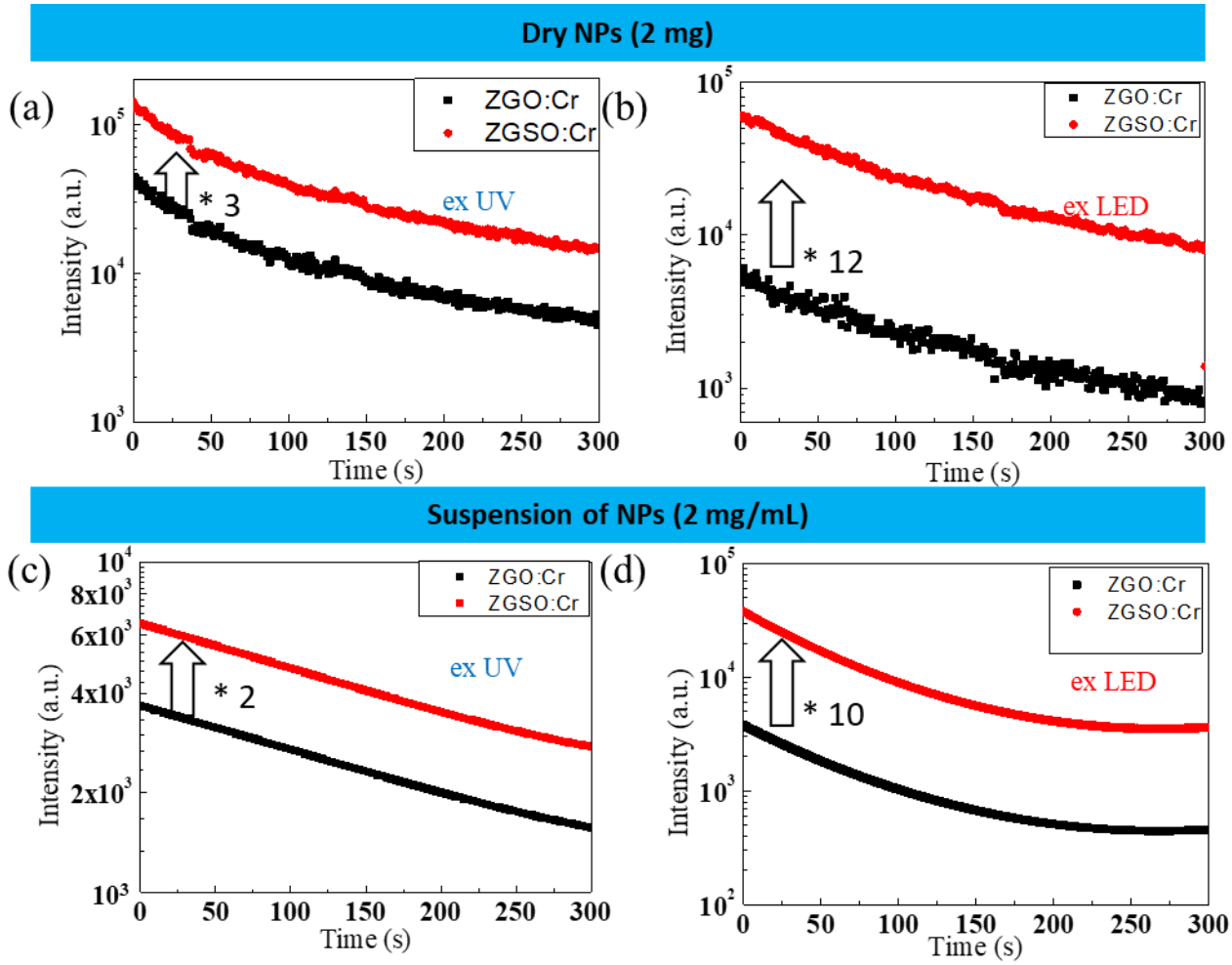

Fig. 3. (a-b) PersL decay of ZGO:Cr (black curve) and ZGSO:Cr NPs (red curve) in dry NPs form (2 mg) after removal of UV (a) and LED (b) excitation. (c-d) PersL decay of ZGO:Cr (black curve) and ZGSO:Cr NPs (red curve) in suspension at 2 mg/mL after removal of UV (c) and LED (d) excitation. For all samples, the acquisition starts 1 min after removal of excitation by UV or visible orange LED light. (The LED emission is shown by Fig. S2 in supplementary information.)

3.4 Deep tissue imaging

In the previous section, we have studied the PersL properties of the two kinds of NPs namely ZGSO:Cr and ZGO:Cr either in dry powders form or dispersed into water suspension. In the following, we will first model bio-imaging by covering the PersL NPs suspension by one piece of pork tissue with a thickness of ~ 2 mm. As before, herein, we tested two

different ways of imaging tissue. At first with pre-excitation for charging the PersL materials, as it can provide an efficient and direct photo excitation of NPs by UV light (see Fig. 4 a). PersL NPs in suspension with UV pre-excitation or LED excitation show afterglow decay curves (with 5 min time collection, Cr^{3+} emission at ~700 nm for the $^2E \rightarrow {}^4A_2$ emission) as presented in in Fig. 4 b. As expected, the initial PersL signals of ZGSO:Cr NPs are stronger than for ZGO:Cr NPs. The *in situ* re-excitation way, using relatively orange LED light (see insert Fig. S2) is shown in Fig. 4 c-d. As a result, when comparing the PersL of the two PersL suspensions for *in situ* excited tissue imaging, the detectable PersL signal for ZGSO:Cr NPs is ~7 times stronger than ZGO:Cr NPs. Second, in an additional way, the visible orange LED light can be used as pre-excitation source as well, as shown in Fig. S7, producing also a stronger PersL signal for ZGSO:Cr NPs suspension compared to the ZGO:Cr NPs.

To sum up, both excitation methods presented in Fig. 4 can be successfully used for PersL bioimaging. Generally, with the UV pre-charging strategy several minutes are required before starting acquisition and the initial PersL signal is lost and unavailable. The *in situ* excitation method is beneficial for repeatability and suitable for the long-term monitoring and imaging using excitation light with good penetration in tissues.

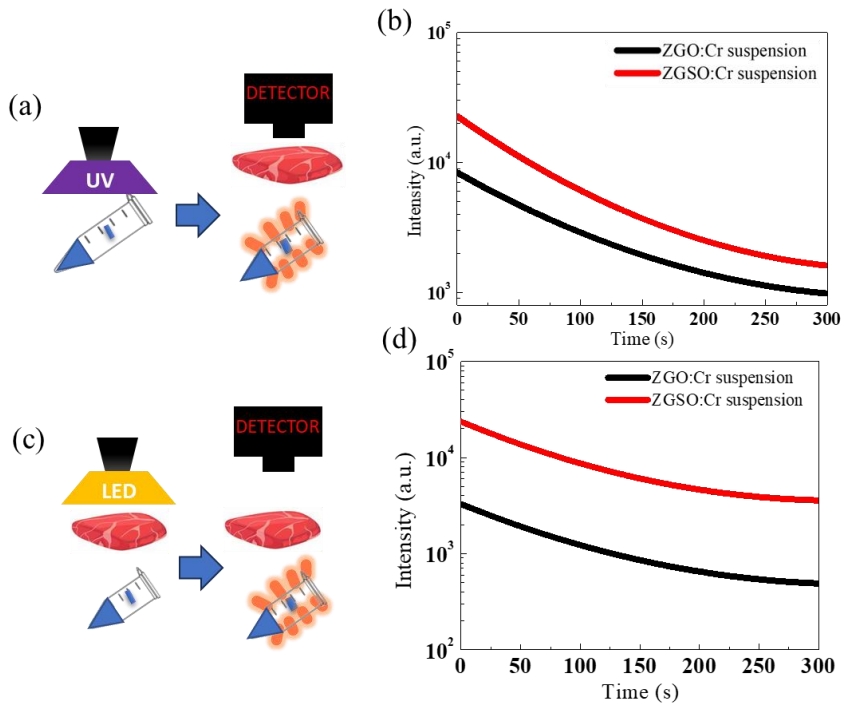

Fig. 4. (a) Schematic of pork tissue imaging based on PersL NPs *via* UV pre-excitation of NPs, and (b) the decay curve of ZGO:Cr^{3+} and ZGSO:Cr^{3+} NPs suspension after covering with tissue; (c) Schematic of pork tissue imaging based on PersL NPs *via in situ* excitation with visible orange LED light through one piece of tissue. (d) Decay curves of ZGO:Cr^{3+} and ZGSO:Cr^{3+} NPs in suspension at 700 nm through one piece of tissue.

Furthermore, to mimic a little more animal experiments, we have investigated the impact of the tissue thickness on the PersL signal (Fig. S3). Noticed that several tissue slices, each of them with a thickness of 2 mm, were used in the study. Here, only ZGSO:Cr^{3+} NPs have been used, due to their better efficiency and the measurements were done using either the UV pre-excitation strategy (Fig. 5 a-b) or *in situ* through tissue LED excitation (Fig. 5 c-d). The observations revealed that, as expected, the PersL intensity decreased as the number of tissue layers covering the PersL probes increases (from 1 to 3 pieces of tissues). In the case of UV pre-excitation (Fig. 5a-b), even with approximately 6 mm of tissue (3 pieces) covering the probes, the NIR PersL signal remained clearly detectable during the 5-minutes acquisition. For thicker tissues, Fig. S5 represents the PersL decay curves of ZGSO:Cr^{3+} NPs in suspension at different depth (even 16 mm and 32 mm) covered by tissues after UV pre-excitation. Additionally, tissue imaging after *in situ* visible/orange LED light excitation

are demonstrated in Fig. 5 c-d. As before, the study evaluates the PersL intensity by varying the tissue thicknesses, ranging from 2 mm to 32 mm (see more information in Fig. S3 and S4 in supplementary). As expected, the intensity decreases when increasing the thickness of the covering tissue. This attenuation is well attributed to the tissue's absorption and scattering properties, which limit the PersL signal propagation through thicker layers (Fig. S3). Fig. S4 shows the PersL decay curves of ZGSO:Cr^{3+} NPs and ZGO:Cr^{3+} NPs in suspension with different penetration depths and limitation of tissue imaging *via* visible orange LED light *in situ* excitation. A detection of the signal through about 20 mm of tissue thickness is possible using ZGO:Cr^{3+} NPs. The signal detection increases up to 32 mm with the ZGSO:Cr^{3+} NPs suspension. These depth limitations are measured using suspension with NPs concentration of 2 mg/mL in 1mL volume. Note that this depth limitation is also controlled by the sensitivity of the detection devices. However for all cases, ZGSO:Cr^{3+} is more appropriate than ZGO:Cr^{3+} for deep tissue imaging.

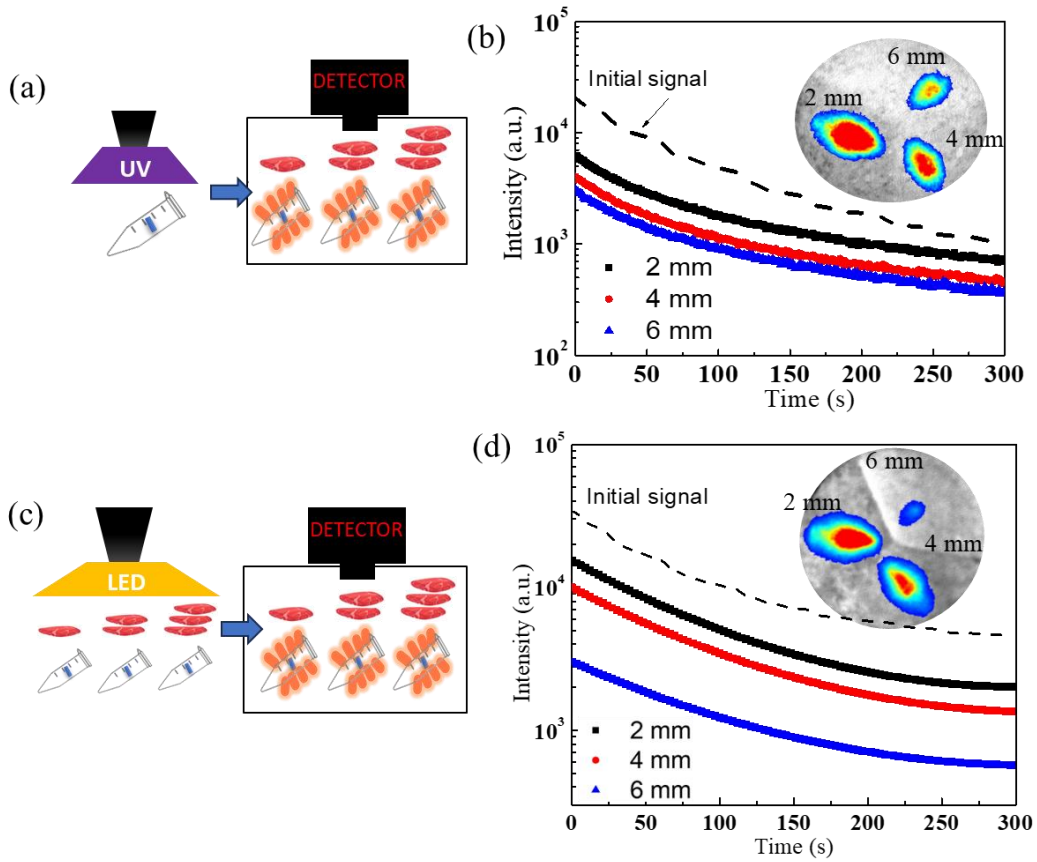

Fig. 5. (a) Principle of PersL excitation of ZGSO:Cr^{3+} NPs *via* (a) UV pre-excitation then tissue covering or (c) *in situ* excitation with visible orange LED light through tissue. (b, d) PersL signal detection through different tissue thickness, using UV pre-excitation (b) or visible/orange LED light *in situ* excitation method (d), respectively (drops at about 20s is due to experimental apparatus).

3.5 In vivo imaging with mice using pristine particles

In the following part, we have performed *in vivo* imaging experiments to further explore the performances of both PersL NPs. In a first experiment, mice were injected with 200 µL of 10 mg/mL ZGO:Cr^{3+} NPs or ZGSO:Cr^{3+} NPs pre-excited with UV. Both NPs have a hydrodynamic diameter of approximately 90 nm and exhibited slightly positive surface charge (15 ± 2mV for ZGO and 5 ± 1mV for ZGSO NPs). Images presented in Fig. 6 a and data analysis based on UV pre-excitation revealed that mice injected with ZGSO:Cr NPs produce stronger PersL signal in comparison to those injected with ZGO:Cr NPs, as shown in Fig. 6 b. *Ex vivo* imaging was performed 4 hours after injection, and as expected with non-functionalized NPs, most of the PersL signal was detected in the liver (Fig. 6 c). A PersL signal about 7 times stronger from the liver containing ZGSO:Cr NPs is obtained, emphasizing their superior PersL properties and detectability, compared to ZGO:Cr NPs, as shown in Fig. 6 d.

To demonstrate the advantage of ZGSO:Cr NPs using *in situ* excitation for *in vivo* imaging, a second group of mice was injected with ZGSO:Cr NPs and ZGO:Cr NPs and then excited with the visible orange LED light source. Resulting images (Fig. 6 e) and data analysis (Fig. 6 f) show again a stronger PersL signal in mice injected with ZGSO:Cr NPs, with an initial intensity of ~6×10^6 counts, compared to those injected with ZGO:Cr NPs (initial intensity ~8×10^5 counts). Again, *ex vivo* images show that most of the PersL signal after 4 hours was detected in the liver (Fig. 6 g), with approximately 10 times stronger PersL for ZGSO:Cr NPs in comparison to ZGO:Cr NPs (Fig. 6 h).

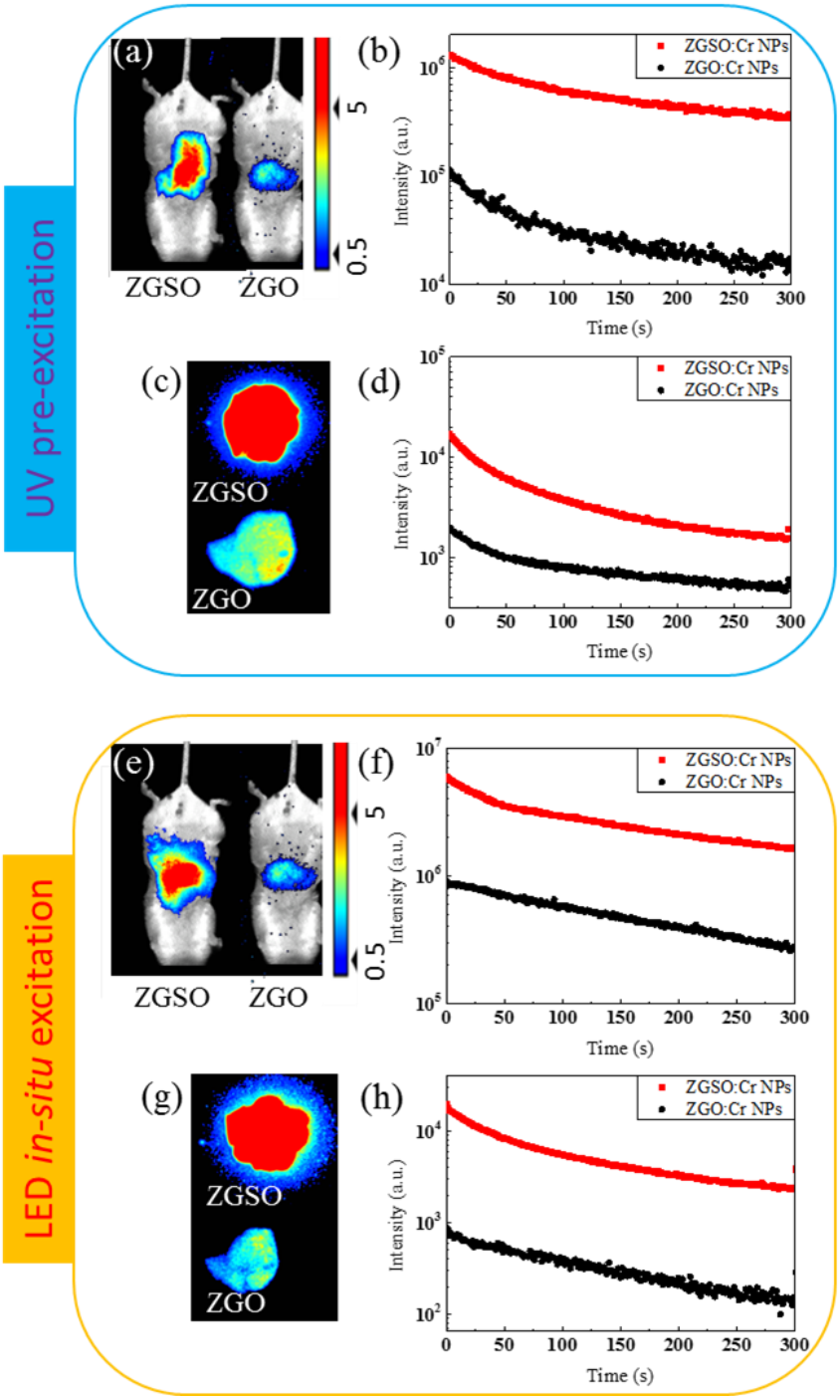

Fig. 6. (a) *In vivo* PersL decays of ZGO:Cr NPs and ZGSO:Cr NPs. (b) PersL decays of ZGO:Cr NPs and ZGSO:Cr NPs. (c) *Ex vivo* imaging results and (d) PersL decay based on ZGO:Cr NPs and ZGSO:Cr NPs. (e) *in vivo* imaging results, using in situ LED excitation, and (f) PersL decays, (g-h) *Ex vivo* imaging results based on ZGO:Cr NPs and ZGSO:Cr

NPs and PersL decay. Notice that the LED excitation is 70 W versus 6 W for the UV lamp (see Figure S2).

3.5 In vivo imaging using PEGylated particles and biodistribution study.

It's well known that surface functionalization of NPs can prolong their residence time in the bloodstream [56-61]. In this study, we used an already established method for obtaining PEG-coated PersL NPs, as described in our previous works [41, 62]. The surface modification involved a two steps process, resulting in the preparation of first NPs-NH_2 and then NPs-PEG. We assessed the size and surface charge of both functionalized NPs (ZGSO and ZGO) using Dynamic Light Scattering (DLS). The results showed a size increase at each step of the synthesis: from 80 (± 5) nm for ZGO:Cr^{3+} to 150 (± 5) nm for ZGO:Cr-NH_2, and further to 250 (± 5) nm for ZGO:Cr-PEG. Similarly, the size of ZGSO:Cr^{3+} NPs increased from 90 (± 5) nm for ZGSO:Cr to 170 (± 5) nm for ZGSO:Cr-NH_2, and finally to 290 (± 5) nm for ZGSO:Cr-PEG (Fig. 7 a-b). These size variations indicate successful chemical surface modification at each step. Additionally, the zeta potential of the PersL NPs evolved from +15 (± 1) mV for ZGO:Cr^{3+} to +30 (± 1) mV for ZGO:Cr-NH_2 and ~ 0 mV for ZGO:Cr-PEG (Fig. 7 c). The same trend was observed for ZGSO:Cr^{3+} NPs, with a change from +5 (± 1) mV to +15 (± 1) mV for ZGSO:Cr-NH_2 and finally ~ 0 mV for ZGSO:Cr-PEG (Fig. 7 d). To further confirm the success of the coating and to quantify the amount of PEG grafted onto PersL NPs, we have used thermogravimetric analysis (TGA). The results, shown in Fig. 7 (e-f), indicate a weight loss of approximately 3% for both ZGO:Cr-NH_2 NPs and ZGSO:Cr-NH_2 NPs. For the second step, ZGO:Cr-PEG NPs exhibited a weight loss of approximately 12.5%, and ZGSO:Cr-PEG NPs showed a weight loss of approximately 16%. Finally, TEM images reveal, with the PEG coating, a ~ 5 nm thickness of "shell" on the NPs of both ZGO:Cr-PEG (ZGO:Cr@PEG) NPs (Fig. 7 g) and ZGSO:Cr-PEG (ZGSO:Cr@PEG) NPs (Fig. 7 h). These findings collectively demonstrate successful functionalization of both types of PersL NPs.

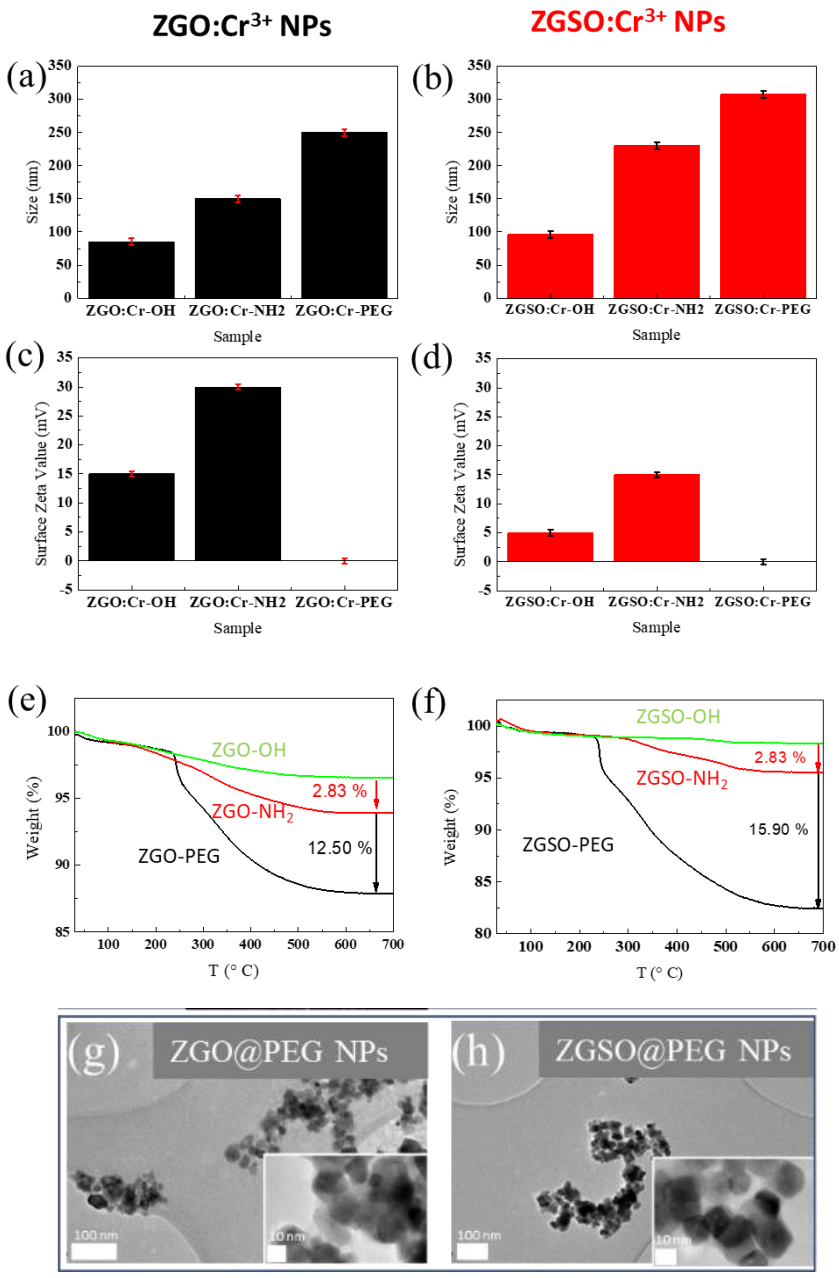

Fig. 7 (a,b) Size (DLS), (c,d) surface zeta potential and (e,f) thermogravimetric results of ZGO:Cr and ZGSO:Cr NPs after each functionalization steps. TEM images of (g) ZGO:Cr-PEG NPs and (h) ZGSO:Cr-PEG NPs with size diameter 30 nm (including ~ 20 nm of ZGO:Cr / ZGSO:Cr core and ~ 5 nm thickness of PEG coating shell, respectively). The illustrations are partial enlargement of the TEM images.

When comparing the two types of suspensions, each containing PersL NPs coated with PEG at a concentration of 10 mg/mL, we observed a noteworthy difference in the PersL signal

strength. Specifically, after UV pre-excitation, the ZGSO:Cr@PEG suspension exhibited a PersL signal that was ~6 times more robust than the ZGO@PEG suspension, as depicted in Fig. S6 (a). Additionally, the use of visible orange LED light excitation provides compelling evidence for the superior PersL properties of ZGSO:Cr@PEG PersL NPs. Fig. S6 (b) displays the NIR PersL decay of ZGO:Cr@PEG and ZGSO:Cr@PEG PersL NPs in suspension, demonstrating a PersL signal strength more than 10 times stronger for the ZGSO:Cr@PEG suspension compared to the ZGO:Cr@PEG suspension. These findings are attributed to the enhanced performance of ZGSO:Cr@PEG NPs, further underlined by the use of a potent visible/orange LED light excitation source. Considering that ZGSO:Cr^{3+} NPs present improved PersL performances and good sensitivity to visible orange LED light excitation, which are two significant advantages, we finally confirmed their superiority for *in vivo* use by conducting further *in vivo* imaging experiments with a detailed comparison of both PEGylated ZGSO:Cr^{3+} and ZGO:Cr^{3+} NPs (10 mg/mL × 200 µL). We found that coated NPs are well circulating into the mice body 1 hour after *in vivo* injection (Fig 8 a), which is a good improvement, compared to the uncoated NPs, rapidly captured by liver (Fig. 6 a and e). Even 4 hours after injection, a strong PersL signal can be detected in all the mice body after a visible orange LED light *in situ* excitation. Remarkably, the decay curve shows that ZGSO:Cr^{3+}@PEG emits a consistently higher initial PersL signal 1 hour (Fig. 8 b) and 4 hours (Fig. 8 c) after *in vivo* injection, compared to the ZGO:Cr^{3+}@PEG. This simple illumination with orange light, even across living tissues, is sufficient to efficiently activate ZGSO:Cr^{3+}-PEG NPs.

The red-shifted excitation spectrum of ZGSO:Cr^{3+} NPs (seen in Fig. 2 a) covers well the orange range which leads to a better efficiency of this excitation. As a result, this PersL imaging probes show advantages for *in vivo* imaging properties not only with *in situ* re-excitation, but also using visible orange LED light as a pre-excitation source (Figs. S7 – S8 in supplementary). The mice injected with ZGSO:Cr^{3+} NPs exhibited over 5 times higher signal intensity, underscoring the advantageous sensitivity of these NPs to visible orange LED light sources.

Importantly, the *in situ* triggering of PersL also enabled *ex vivo* absolute optical quantification. This work revealed a predominant localization of both ZGSO:Cr^{3+}-PEG NPs (Fig. 8 d) and ZGO:Cr^{3+}-PEG NPs (Fig. 8 e) in the liver (left part of the images), with

limited uptake by the spleen. For example, see the ~ 6 times stronger PersL from the liver with ZGSO:Cr^{3+} NPs. This factor is in good agreement with the PersL intensity difference between the equivalent ZGSO: Cr^{3+}-PEG and ZGO: Cr^{3+}-PEG PersL NPs as seen in Fig. S6 (a).

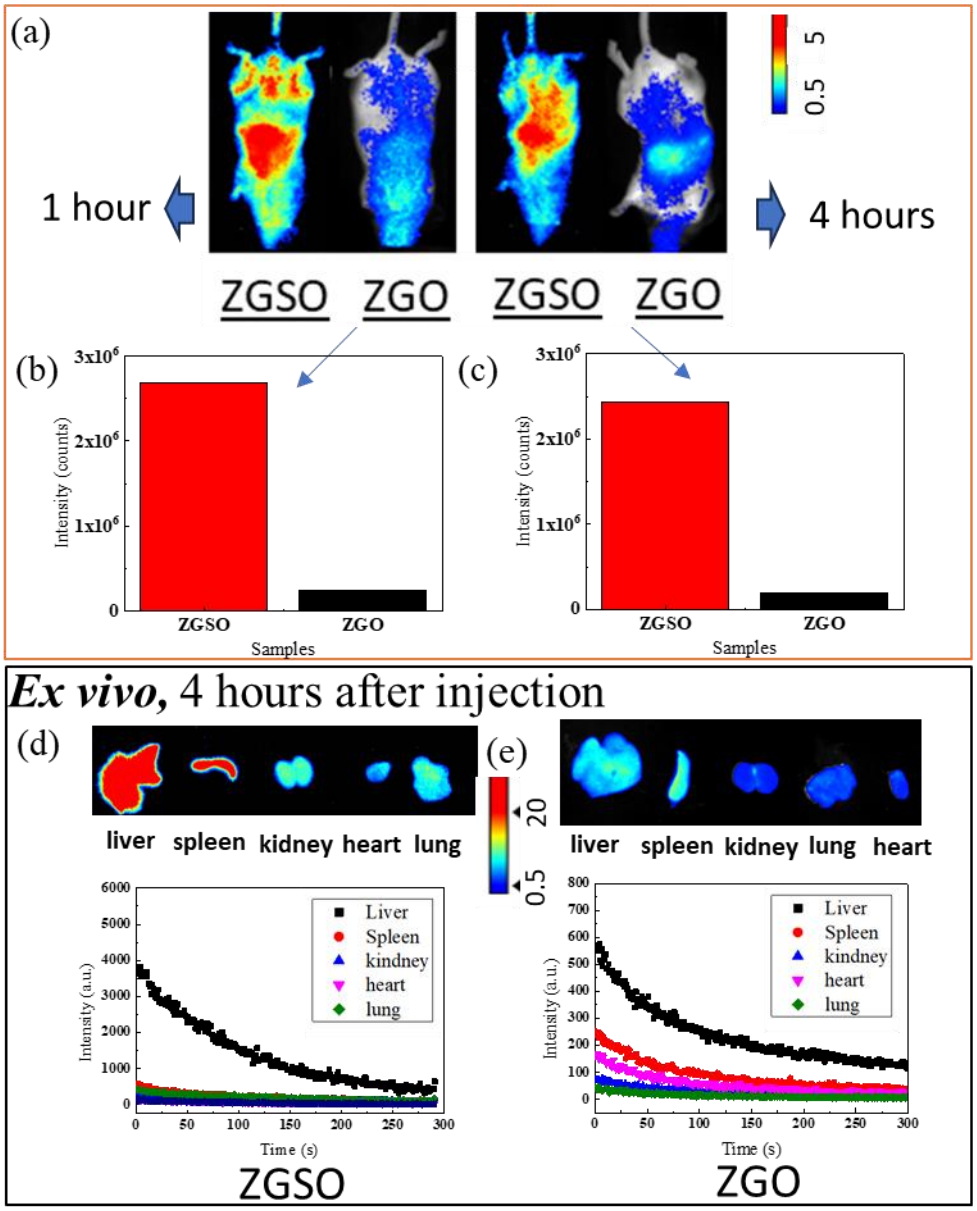

Fig.8. (a) Biodistribution of ZGSO:Cr@PEG NPs and ZGO:Cr@PEG NPs 1h and 4h after injection using the *in situ* LED light excitation. (b-c) PersL in vivo imaging based on ZGSO:Cr@PEG NPs and ZGO:Cr@PEG NPs at 1h (b) or 4h (c) after injection, with *in situ*

519 re-excitation. (d-e) *ex vivo* imaging measurements in the different organs, 4h after injection
520 of ZGSO:Cr@PEG NPs (d) and ZGO:Cr@PEG NPs (e).

521 **4. Conclusions**

522 Nanoscale $Zn_{1.33}Ga_{1.335}Cr_{0.005}Sn_{0.33}O_4$ ($ZGSO:Cr^{3+}$) material was successfully
523 synthesized by hydrothermal method with subsequent annealing and milling process
524 allowing getting 20 nm nanoparticles (measured by TEM). The optical performances of
525 such NPs have been compared to the original $ZGO:Cr^{3+}$ NPs prepared using the same
526 procedure. Both $ZGSO:Cr^{3+}$ and $ZGO:Cr^{3+}$ NPs exhibit PersL emission, stemming from the
527 $^2E \rightarrow {}^4A_2$ (Cr^{3+}) transition, around 700 nm in the deep red/near-infrared (NIR) range.
528 Notably, $ZGSO:Cr^{3+}$ NPs feature a red-shifted excitation spectrum that aligns well with the
529 prominent emission wavelength of visible orange LED lights. This advantageous spectral
530 overlap enhances the *in situ* excitability of PersL, particularly when illuminated with a
531 visible orange LED light, which boasts good tissue penetration capabilities. Consequently,
532 $ZGSO:Cr^{3+}$ NPs demonstrate a more robust PersL emission due to their adept
533 responsiveness to the powerful LED excitation source, showcasing superior sensitivity to
534 orange LED light irradiation, and harboring a higher concentration of traps compared to
535 $ZGO:Cr^{3+}$ NPs.

536 Deep tissues imaging and *in vivo* imaging results show that $ZGSO:Cr^{3+}$ exhibit slightly
537 enhanced (factor ~ 3) NIR emission intensity after UV excitation compared to $ZGO:Cr^{3+}$.
538 More interestingly, when using visible orange LED light excitation, the signal intensity of
539 $ZGSO:Cr^{3+}$ is much higher (factor > 10) than $ZGO:Cr^{3+}$. Thus, within the same situation,
540 $ZGSO:Cr^{3+}$ is a better choice for deeper tissue *in vivo* imaging than original $ZGO:Cr^{3+}$. The
541 depth limitation of the *in situ* excited deep tissue imaging reaches 32 mm for $ZGSO:Cr^{3+}$
542 NPs suspension, with a worthily notable improvement, compared to 20 mm for $ZGO:Cr^{3+}$
543 NPs suspension. Using PEG surface-functionalized NPs, a good distribution of $ZGSO:Cr^{3+}$
544 NPs exhibiting in all animals bodies over at least 4 hours, which indicates a good circulation
545 time in the blood.

546 Facing that X-rays excitation sources for recently proposed PersL nanomaterials [35],
547 such as $NaLnF_4$ [63] $ZGGO:Cr^{3+},Mn^{2+}$ [64] and $LiGa_5O_8:Cr^{3+}$, are limited due to potential
548 health risks, visible orange LED light *in situ* excitation offers a safe and efficient method

for *in situ & in vivo* imaging. Therefore, we believe that visible orange LED light *in situ* excitation of ZGSO:Cr^{3+} NPs have great potential in bioimaging, and should overcome pioneer work using the original ZGO:Cr^{3+} for improved *in vivo* diagnosis.

Author Contributions

G.C., B.V. and C.R. conceived and designed the research. G.C., J.S., T.N. carried out the experiments. J.S. was responsible for biological characterization and small animal in vivo imaging. G.C. responsible for optical and TL characterization and mechanism. All of the authors analyzed the data and discussed the results. G.C., C.C., B.V., and C.R. wrote the manuscript. The authors declare no conflict of interest.

Conflicts of interest

There are no conflicts to declare.

Acknowledgements

This research was funded by Agence Nationale de la Recherche (ANR-22-CE09-0029-01 PLEaSe) and the CSC Grant program. The “plateau technique de caractérisation des solides” and the LIOPA are acknowledged for the experiments.

References

[1] J. Xu, S. Tanabe, Persistent luminescence instead of phosphorescence: History, mechanism, and perspective, Journal of Luminescence 205 (2019) 581-620. https://doi.org/10.1016/j.jlumin.2018.09.047.

[2] W.H. Li, Y.X. Zhuang, P. Zheng, T.L. Zhou, J. Xu, J. Ueda, S. Tanabe, L. Wang, R.J. Xie, Tailoring Trap Depth and Emission Wavelength in Y3Al5-x,GaxO12:Ce3+,V3+ Phosphor-in-Glass Films for Optical Information Storage, Acs Applied Materials & Interfaces 10(32) (2018) 27150-27159. https://doi.org/10.1021/acsami.8b10713.

[3] Y. Katayama, A. Hashimoto, J. Xu, J. Ueda, S. Tanabe, Thermoluminescence investigation on Y3Al5-xGaxO12: Ce3+-Bi3+ green persistent phosphors, Journal of Luminescence 183 (2017) 355-359. https://doi.org/10.1016/j.jlumin.2016.11.074.

[4] Y. Katayama, B. Viana, D. Gourier, J. Xu, S. Tanabe, Photostimulation induced persistent luminescence in Y3Al2Ga3O12:Cr3+, Optical Materials Express 6(4) (2016) 1405-1413. https://doi.org/10.1364/ome.6.001405.

[5] M. Mori, J. Xu, G. Okada, T. Yanagida, J. Ueda, S. Tanabe, Comparative study of optical and scintillation properties of Ce:YAGG, Ce:GAGG and Ce:LuAGG transparent ceramics, Journal of the Ceramic Society of Japan 124(5) (2016) 569-573. https://doi.org/10.2109/jcersj2.15239.
[6] A.D. Sontakke, J. Ueda, J. Xu, K. Asami, M. Katayama, Y. Inada, S. Tanabe, A Comparison on Ce3+ Luminescence in Borate Glass and YAG Ceramic: Understanding the Role of Host's Characteristics, Journal of Physical Chemistry C 120(31) (2016) 17683-17691. https://doi.org/10.1021/acs.jpcc.6b04159.
[7] X. Ding, Q. Zhang, Multi spectral responsive near infrared-II broad emission material and its LED device and imaging research, Ceramics International 47(24) (2021) 34851-34859. https://doi.org/10.1016/j.ceramint.2021.09.026.
[8] V.F. Guimaraes, A.D. Sontakke, L.J.Q. Maia, M. Salaun, I. Gautier-Luneau, A. Ferrier, B. Viana, A. Ibanez, Photoluminescence properties of glassy yttrium aluminum borate powders: Dopant-free phosphors for solid-state lighting, Journal of Luminescence 188 (2017) 448-453. https://doi.org/10.1016/j.jlumin.2017.05.013.
[9] S. Fujita, S. Tanabe, Glass-Ceramics and Solid-State Lighting, International Journal of Applied Glass Science 6(4) (2015) 356-363. https://doi.org/10.1111/ijag.12143.
[10] V.F. Guimaraes, M. Salaun, P. Burner, L.J.Q. Maia, A. Ferrier, B. Viana, I. Gautier-Luneau, A. Ibanez, Controlled preparation of aluminum borate powders for the development of defect-related phosphors for warm white LED lighting, Solid State Sciences 65 (2017) 6-14. https://doi.org/10.1016/j.solidstatesciences.2016.12.011.
[11] Q. Le Masne de Chermont, C. Chanéac, J. Seguin, F. Pellé, S. Maîtrejean, J.-P. Jolivet, D. Gourier, M. Bessodes, D. Scherman, Nanoprobes with near-infrared persistent luminescence for in vivo imaging, Proceedings of the National Academy of Sciences 104(22) (2007) 9266-9271.
[12] C. Rosticher, B. Viana, T. Maldiney, C. Richard, C. Chanéac, Persistent luminescence of Eu, Mn, Dy doped calcium phosphates for in-vivo optical imaging, Journal of Luminescence 170 (2016) 460-466.
[13] T. Maldiney, D. Scherman, C. Richard, Persistent luminescence nanoparticles for diagnostics and imaging, Functional Nanoparticles for Bioanalysis, Nanomedicine, and Bioelectronic Devices Volume 2, ACS Publications2012, pp. 1-25.
[14] J. Liu, T. Lécuyer, J. Seguin, N. Mignet, D. Scherman, B. Viana, C. Richard, Imaging and therapeutic applications of persistent luminescence nanomaterials, Advanced drug delivery reviews 138 (2019) 193-210.
[15] B. Viana, C. Richard, V. Castaing, E. Glais, M. Pellerin, J. Liu, C. Chanéac, NIR-persistent luminescence nanoparticles for bioimaging, principle and perspectives, Near Infrared-Emitting Nanoparticles for Biomedical Applications (2020) 163-197.
[16] R.Y. Jiang, J. Yang, Y.Q. Meng, D.T. Yan, C.G. Liu, C.S. Xu, Y.X. Liu, X-ray/red-light excited ZGGO:Cr,Nd nanoprobes for NIR-I/II afterglow imaging, Dalton Transactions 49(18) (2020) 6074-6083. https://doi.org/10.1039/d0dt00247j.
[17] J. Tang, Y. Su, D. Deng, L. Zhang, N. Yang, Y. Lv, A persistent luminescence microsphere-based probe for convenient imaging analysis of dopamine, Analyst 141(18) (2016) 5366-5373.
[18] B.-Y. Wu, X.-P. Yan, Bioconjugated persistent luminescence nanoparticles for Föster resonance energy transfer immunoassay of prostate specific antigen in serum and cell extracts without in situ excitation, Chemical Communications 51(18) (2015) 3903-3906.
[19] N. Li, Y. Li, Y. Han, W. Pan, T. Zhang, B. Tang, A highly selective and instantaneous nanoprobe for detection and imaging of ascorbic acid in living cells and in vivo, Analytical chemistry 86(8) (2014) 3924-3930.

[20] B.-Y. Wu, H.-F. Wang, J.-T. Chen, X.-P. Yan, Fluorescence resonance energy transfer inhibition assay for α-fetoprotein excreted during cancer cell growth using functionalized persistent luminescence nanoparticles, Journal of the American Chemical Society 133(4) (2011) 686-688.
[21] D. Li, T.T. Wang, L. Li, L.Y. Zhang, C.G. Wang, X.T. Dong, Designed formation of Prussian Blue/CuS Janus nanostructure with enhanced NIR-I and NIR-II dual window response for tumor thermotherapy, Journal of Colloid and Interface Science 613 (2022) 671-680. https://doi.org/10.1016/j.jcis.2022.01.074.
[22] C.R. Bruno Viana, Victor Castaing, Estelle Glais, Morgane Pellerin, Jianhua Liu, Corinne Chanéac, NIR-Persistent Luminescence Nanoparticles for Bioimaging, Principle and Perspectives, Springer2020.
[23] L. Tang, X.D. Zeng, H. Zhou, C.H. Gui, Q.L. Luo, W.Y. Zhou, J. Wu, Q.Q. Li, Y. Li, Y.L. Xiao, Theranostic Gold Nanoclusters for NIR-II Imaging and Photodynamic Therapy, Chemical Research in Chinese Universities 37(4) (2021) 934-942. https://doi.org/10.1007/s40242-021-1117-3.
[24] Z. Yan, M. Sun, M. Wang, C. Yin, Z.-J. Wei, Z. Zhang, Y. Wang, W. Wang, Z. Yuan, Single-laser excitation synergistic photo-and chemodynamic therapy system based on persistent luminescence nanoparticles, Journal of Controlled Release 364 (2023) 371-382.
[25] Q. Wang, N. Liu, Z. Hou, J. Shi, X. Su, X. Sun, Radioiodinated persistent luminescence nanoplatform for radiation-induced photodynamic therapy and radiotherapy, Advanced healthcare materials 10(5) (2021) 2000802.
[26] M.H. Chan, W.T. Huang, J. Wang, R.S. Liu, M. Hsiao, Next-Generation Cancer-Specific Hybrid Theranostic Nanomaterials: MAGE-A3 NIR Persistent Luminescence Nanoparticles Conjugated to Afatinib for In Situ Suppression of Lung Adenocarcinoma Growth and Metastasis, Advanced Science 7(9) (2020) 1903741.
[27] R. Abdurahman, C.-X. Yang, X.-P. Yan, Conjugation of a photosensitizer to near infrared light renewable persistent luminescence nanoparticles for photodynamic therapy, Chemical Communications 52(90) (2016) 13303-13306.
[28] L. Song, P.P. Li, W. Yang, X.H. Lin, H. Liang, X.F. Chen, G. Liu, J. Li, H.H. Yang, Low-dose X-ray activation of W (VI)-doped persistent luminescence nanoparticles for deep-tissue photodynamic therapy, Advanced Functional Materials 28(18) (2018) 1707496.
[29] G.Y. Cai, T. Delgado, C. Richard, B. Viana, ZGSO Spinel Nanoparticles with Dual Emission of NIR Persistent Luminescence for Anti-Counterfeiting Applications, Materials 16(3) (2023). https://doi.org/10.3390/ma16031132.
[30] X.W. Yu, H.Y. Zhang, J.H. Yu, Luminescence anti-counterfeiting: From elementary to advanced, Aggregate 2(1) (2021) 20-34. https://doi.org/10.1002/agt2.15.
[31] J.J. Wei, Y.Y. Liu, M.R. Zhang, W. Zheng, P. Huang, Z.L. Gong, R.F. Li, X.Y. Chen, Blue-LED-excitable NIR-II luminescent lanthanide-doped SrS nanoprobes for ratiometric thermal sensing, Science China-Materials 65(4) (2022) 1094-1102. https://doi.org/10.1007/s40843-021-1801-8.
[32] M.R. Zhang, W. Zheng, Y. Liu, P. Huang, Z.L. Gong, J.J. Wei, Y. Gao, S.Y. Zhou, X.J. Li, X.Y. Chen, A New Class of Blue-LED-Excitable NIR-II Luminescent Nanoprobes Based on Lanthanide-Doped CaS Nanoparticles, Angewandte Chemie-International Edition 58(28) (2019) 9556-9560. https://doi.org/10.1002/anie.201905040.
[33] J. Wiedenmann, F. Oswald, G.U. Nienhaus, Fluorescent Proteins for Live Cell Imaging: Opportunities, Limitations, and Challenges, Iubmb Life 61(11) (2009) 1029-1042. https://doi.org/10.1002/iub.256.

[34] T. Maldiney, G. Sraiki, B. Viana, D. Gourier, C. Richard, D. Scherman, M. Bessodes, K. Van den Eeckhout, D. Poelman, P.F. Smet, In vivo optical imaging with rare earth doped Ca 2 Si 5 N 8 persistent luminescence nanoparticles, Optical Materials Express 2(3) (2012) 261-268.
[35] C. Richard, B. Viana, Persistent X-ray-activated phosphors: mechanisms and applications, Light Sci Appl 11(1) (2022) 123. https://doi.org/10.1038/s41377-022-00808-6.
[36] A. Abdukayum, J.-T. Chen, Q. Zhao, X.-P. Yan, Functional Near Infrared-Emitting Cr3+/Pr3+ Co-Doped Zinc Gallogermanate Persistent Luminescent Nanoparticles with Superlong Afterglow for in Vivo Targeted Bioimaging, Journal of the American Chemical Society 135(38) (2013) 14125-14133. https://doi.org/10.1021/ja404243v.
[37] Y. Katayama, B. Viana, D. Gourier, J. Xu, S. Tanabe, Photostimulation induced persistent luminescence in Y_3Al_2Ga_3O_12:Cr^3+, Optical Materials Express 6(4) (2016). https://doi.org/10.1364/ome.6.001405.
[38] P.D. Rack, J.J. Peterson, M.D. Potter, W. Park, Eu+ 3 and Cr+ 3 doping for red cathodoluminescence in ZnGa 2 O 4, Journal of Materials Research 16 (2001) 1429-1433.
[39] X. Fu, C. Liu, J. Shi, H. Man, J. Xu, H. Zhang, Long persistent near infrared luminescence nanoprobes LiGa5O8: Cr3+-PEG-OCH3 for in vivo imaging, Optical Materials 36(11) (2014) 1792-1797.
[40] T. Maldiney, B. Viana, A. Bessière, D. Gourier, M. Bessodes, D. Scherman, C. Richard, In vivo imaging with persistent luminescence silicate-based nanoparticles, Optical Materials 35(10) (2013) 1852-1858.
[41] T. Maldiney, A. Bessiere, J. Seguin, E. Teston, S.K. Sharma, B. Viana, A.J.J. Bos, P. Dorenbos, M. Bessodes, D. Gourier, D. Scherman, C. Richard, The in vivo activation of persistent nanophosphors for optical imaging of vascularization, tumours and grafted cells, Nature Materials 13(4) (2014) 418-426. https://doi.org/10.1038/nmat3908.
[42] Y. Jiang, Y. Li, C. Richard, D. Scherman, Y. Liu, Hemocompatibility investigation and improvement of near-infrared persistent luminescent nanoparticle ZnGa2O4:Cr3+ by surface PEGylation, J Mater Chem B 7 (2019). https://doi.org/10.1039/c9tb00378a.
[43] T. Lecuyer, J. Seguin, A. Balfourier, M. Delagrange, P. Burckel, R. Lai-Kuen, V. Mignon, B. Ducos, M. Tharaud, B. Saubamea, D. Scherman, N. Mignet, F. Gazeau, C. Richard, Fate and biological impact of persistent luminescence nanoparticles after injection in mice: a one-year follow-up, Nanoscale 14(42) (2022) 15760-15771. https://doi.org/10.1039/d2nr03546d.
[44] L. Giordano, G.Y. Cai, J. Seguin, J.H. Liu, C. Richard, L.C.V. Rodrigues, B. Viana, Persistent Luminescence Induced by Upconversion: An Alternative Approach for Rechargeable Bio-Emitters, Advanced Optical Materials. https://doi.org/10.1002/adom.202201468.
[45] C. Matuszewska, T.W. Pańczuk, P.A. Tanner, K.L. Wong, Optimization of persistent luminescence performance of zinc gallogermanates, Materials Today Chemistry 26 (2022) 101065. https://doi.org/https://doi.org/10.1016/j.mtchem.2022.101065.
[46] Z.F. Pan, V. Castaing, L.P. Yan, L.L. Zhang, C. Zhang, K. Shao, Y.F. Zheng, C.K. Duan, J.H. Liu, C. Richard, B. Viana, Facilitating Low-Energy Activation in the Near-Infrared Persistent Luminescent Phosphor Zn1+xGa2-2xSnxO4:Cr3+ via Crystal Field Strength Modulations, Journal of Physical Chemistry C 124(15) (2020) 8347-8358. https://doi.org/10.1021/acs.jpcc.0c01951.
[47] M. Allix, S. Chenu, E. Véron, T. Poumeyrol, E.A. Kouadri-Boudjelthia, S. Alahrache, F. Porcher, D. Massiot, F. Fayon, Considerable improvement of long-persistent luminescence in germanium and tin substituted ZnGa2O4, Chemistry of Materials 25(9) (2013) 1600-1606.
[48] A. Bessiere, S. Jacquart, K. Priolkar, A. Lecointre, B. Viana, D. Gourier, ZnGa2O4:Cr3+: a new red long-lasting phosphor with high brightness, Optics Express 19(11) (2011) 10131-10137. https://doi.org/10.1364/oe.19.010131.

[49] G. Cai, L. Giordano, C. Richard, B. Viana, Effect of the Elaboration Method on Structural and Optical Properties of Zn1.33Ga1.335Sn0.33O4:0.5%Cr3+ Persistent Luminescent Nanomaterials, Nanomaterials 13(15) (2023) 2175.
[50] D. Gourier, A. Bessiere, S.K. Sharma, L. Binet, B. Viana, N. Basavaraju, K.R. Priolkar, Origin of the visible light induced persistent luminescence of Cr3+ -doped zinc gallate, Journal of Physics and Chemistry of Solids 75(7) (2014) 826-837. https://doi.org/10.1016/j.jpcs.2014.03.005.
[51] J. Ueda, M. Back, M.G. Brik, Y. Zhuang, M. Grinberg, S. Tanabe, Ratiometric optical thermometry using deep red luminescence from 4T2 and 2E states of Cr3+ in ZnGa2O4 host, Optical Materials 85 (2018) 510-516.
[52] K. Van den Eeckhout, P.F. Smet, D. Poelman, Persistent luminescence in Eu2+-doped compounds: a review, Materials 3(4) (2010) 2536-2566.
[53] F. Urbach, Zur lumineszenz der alkalihalogenide, Sitzungsberichte Akad. der Wiss. Wien 139 (1930) 363-372.
[54] J.T. Randall, M.H.F. Wilkins, Phosphorescence and electron traps-I. The study of trap distributions, Proceedings of the Royal Society of London. Series A. Mathematical and Physical Sciences 184(999) (1945) 365-389.
[55] T.I. Quickenden, J.A. Irvin, The ultraviolet absorption spectrum of liquid water, The Journal of Chemical Physics 72(8) (2008) 4416-4428. https://doi.org/10.1063/1.439733.
[56] D. Dassonville, T. Lécuyer, J. Seguin, Y. Corvis, J. Liu, G. Cai, J. Mouton, D. Scherman, N. Mignet, C. Richard, Zwitterionic Functionalization of Persistent Luminescence Nanoparticles: Physicochemical Characterizations and In Vivo Biodistribution in Mice, Coatings, 2023.
[57] J. Liu, L. Kotrchova, T. Lecuyer, Y. Corvis, J. Seguin, N. Mignet, T. Etrych, D. Scherman, E. Randarova, C. Richard, Coating Persistent Luminescence Nanoparticles With Hydrophilic Polymers forin vivoImaging, Frontiers in Chemistry 8 (2020). https://doi.org/10.3389/fchem.2020.584114.
[58] T. Lecuyer, M.-A. Durand, J. Volatron, M. Desmau, R. Lai-Kuen, Y. Corvis, J. Seguin, G. Wang, D. Alloyeau, D. Scherman, N. Mignet, F. Gazeau, C. Richard, Degradation of ZnGa2O4:Cr3+ luminescent nanoparticles in lysosomal-like medium, Nanoscale 12(3) (2020) 1967-1974. https://doi.org/10.1039/c9nr06867h.
[59] Y. Portilla, S. Mellid, A. Paradela, A. Ramos-Fernández, N. Daviu, L. Sanz-Ortega, S. Pérez-Yagüe, M.P. Morales, D.F. Barber, Iron Oxide Nanoparticle Coatings Dictate Cell Outcomes Despite the Influence of Protein Coronas, ACS Applied Materials & Interfaces 13(7) (2021) 7924-7944. https://doi.org/10.1021/acsami.0c20066.
[60] Q. Lin, P. Fathi, X. Chen, Nanoparticle delivery in vivo: A fresh look from intravital imaging, eBioMedicine 59 (2020) 102958. https://doi.org/https://doi.org/10.1016/j.ebiom.2020.102958.
[61] B.R. Knowles, P. Wagner, S. Maclaughlin, M.J. Higgins, P.J. Molino, Silica Nanoparticles Functionalized with Zwitterionic Sulfobetaine Siloxane for Application as a Versatile Antifouling Coating System, ACS Applied Materials & Interfaces 9(22) (2017) 18584-18594. https://doi.org/10.1021/acsami.7b04840.
[62] T. Maldiney, C. Richard, J. Seguin, N. Wattier, M. Bessodes, D. Scherman, Effect of Core Diameter, Surface Coating, and PEG Chain Length on the Biodistribution of Persistent Luminescence Nanoparticles in Mice, Acs Nano 5(2) (2011) 854-862. https://doi.org/10.1021/nn101937h.
[63] P. Pei, Y. Chen, C.X. Sun, Y. Fan, Y.M. Yang, X. Liu, L.F. Lu, M.Y. Zhao, H.X. Zhang, D.Y. Zhao, X.G. Liu, F. Zhang, X-ray-activated persistent luminescence nanomaterials for NIR-II imaging, Nature Nanotechnology 16(9) (2021) 1011-+. https://doi.org/10.1038/s41565-021-00922-3.

[64] H.M. Jiang, R.P. Wang, Q. Zhang, L. Song, X. Sun, J.P. Shi, Y. Zhang, A dual-functional nanoplatform based on NIR and green dual-emissive persistent luminescence nanoparticles for X-ray excited persistent luminescence imaging and photodynamic therapy, Nanoscale 14(41) (2022) 15451-15461. https://doi.org/10.1039/d2nr03631b.